Received: 26 September 2016 | Revised: 12 May 2017 | Accepted: 28 May 2017

DOI: 10.1002/nag.2712

RESEARCH ARTICLE

WILEY

Numerical analysis of the effect of natural microcracks on the supercritical CO_2 fracturing crack network of shale rock based on bonded particle models

Peihuo Peng[1,2] | Yang Ju[1,3,4] | Yongliang Wang[1,4] | Shaoqin Wang[2] | Feng Gao[3]

[1] School of Mechanics and Civil Engineering, China University of Mining and Technology, Beijing 100083, China

[2] School of Sciences, Beijing University of Civil Engineering and Architecture, Beijing 102612, China

[3] State Key Laboratory for Geomechanics and Deep Underground Engineering, China University of Mining & Technology, Xuzhou 221116, China

[4] State Key Laboratory of Coal Resources and Safe Mining, China University of Mining and Technology, Beijing 100083, China

Correspondence
Yang Ju, State Key Laboratory of Coal Resources and Safe Mining, China University of Mining and Technology, Beijing 100083, China.
Email: juy@cumtb.edu.cn

Funding information
Ministry of Science and Technology of the People's Republic of China, Grant/Award Number: 2016YFC0600705; National Natural Science Foundation of China, Grant/Award Number: 51374213, 51674251, 51125017 and 51608301; Science and Technology Support Program of Jiangsu Province, Grant/Award Number: 2014-27; Priority Academic Program Development of Jiangsu Higher Education Institutions, Grant/Award Number: PAPD 2014; Foundation of Science Project of Beijing Municipal Education Commission, Grant/Award Number: SQKM201610016015; China Postdoctoral Science Foundation, Grant/Award Number: 2016M601170 and 2015M571030

Summary

The problem of predicting the geometric structure of induced fractures is highly complex and significant in the fracturing stimulation of rock reservoirs. In the traditional continuous fracturing models, the mechanical properties of reservoir rock are input as macroscopic quantities. These models neglect the microcracks and discontinuous characteristics of rock, which are important factors influencing the geometric structure of the induced fractures. In this paper, we simulate supercritical CO_2 fracturing based on the bonded particle model to investigate the effect of original natural microcracks on the induced-fracture network distribution. The microcracks are simulated explicitly as broken bonds that form and coalesce into macroscopic fractures in the supercritical CO_2 fracturing process. A calculation method for the distribution uniformity index (DUI) is proposed. The influence of the total number and DUI of initial microcracks on the mechanical properties of the rock sample is studied. The DUI of the induced fractures of supercritical CO_2 fracturing and hydraulic fracturing for different DUIs of initial microcracks are compared, holding other conditions constant. The sensitivity of the DUI of the induced fractures to that of initial natural microcracks under different horizontal stress ratios is also probed. The numerical results indicate that the distribution of induced fractures of supercritical CO_2 fracturing is more uniform than that of common hydraulic fracturing when the horizontal stress ratio is small.

Highlights

- A bonded particle model was used to simulate supercritical CO_2 fracturing of rock.
- The distribution uniformity index (DUI) was proposed to characterize fractures.
- The supercritical CO_2 fracturing processes with different DUIs were analyzed.
- The dependence of fracturing induced cracks on initial microcracks was probed.
- The CO_2 fracturing created more uniformly distributed cracks than hydrofracturing.

KEYWORDS

bonded particle model (BPM), distribution uniformity index (DUI), mechanical properties, natural microcracks, supercritical CO_2 fracturing

1 | INTRODUCTION

Hydraulic fracturing technology has played a critical role in the shale gas revolution in recent years. However, this technology was opposed by environmental protection organizations because of the method's impact on water consumption and environmental quality. Numerous scholars have conducted research studies on all aspects of hydraulic fracturing, including alternative technologies to hydraulic fracturing. In particular, the concept of nonaqueous fracturing has attracted considerable interest. Many studies have indicated that the viscosity of fracturing fluid is lower and that hydraulic fracturing has many more branches and tends to generate a more complex fracture network.[1-4] Supercritical CO_2 has the characteristics of high density, low surface tension, and super low viscosity. Supercritical CO_2 will have broad prospects if used as the fracturing fluid. At present, many scholars from various countries are researching supercritical CO_2 fracturing. Gan et al analyzed the effect of interfacial tension of the fracturing fluid on the breakdown pressure.[5] He et al investigated the pressurization effect during supercritical CO_2 jet fracturing and studied the properties and parametric influences of the supercritical CO_2 jet; their work demonstrated that supercritical CO_2 jetting has a higher impact pressure and velocity than a water jet under the same conditions.[6,7] Jiang et al studied the mechanism of shale microstructure change via supercritical CO_2 treatment and found that supercritical CO_2 can extract more organic matter from the pores and fractures in shale, increasing the number of shale gas seepage channels and enhancing connectivity.[8] Skurtveit et al investigated the basic mechanisms involved in the CO_2 breakthrough process.[9]

Shale gas reservoirs are naturally fractured media, and natural fractures exist in nearly all gas productive shales. During fracturing, propagation of a complex fracture network is developed because of interactions between preexisting natural fractures and hydraulic fractures. In the study of fracturing, the original natural fractures in the reservoir have a significant impact on the fracturing process. Julia et al characterized natural fractures in 4 Barnett Shale cores and noted that the hydraulic fractures can stimulate the natural fractures to open, producing a complex network.[10] Ren et al simulated the process of fracture network propagation in different natural fracture distributions with an modified displacement discontinuity method-based model, and their work showed that more mature natural fractures are beneficial for the formation of the fracture network.[11] Zou et al studied the influence of natural fractures on the generation of the hydraulic fracture network (HFN) through a series of true triaxial fracturing experiments. The experimental results indicated that natural fractures, horizontal stress differences, the fracturing fluid viscosity, and other factors will impact the hydraulic fracture geometry.[12] Zhao conducted a fracturing simulation of a shale gas reservoir with large amounts of natural fractures. The simulation results indicated that the physical property parameters of natural fractures, such as the length, azimuth, dip angle, and density, are key input parameters that impact the geometry and complexity of the HFN.[13]

The natural fractures in the above research all refer to natural macrofractures. The scales of these fractures range from a few millimeters to several meters. In fact, there are various scales of natural fractures in shale reservoirs, including macrofractures and microfractures. Because the preexisting natural macrofractures have a significant influence on both seepage flow and fracturing process, current research studies focus on this type of natural fracture. However, referring to fractures at the microscale, some studies have indicated that shale reservoirs contain many natural microcracks that are randomly distributed.[14-16] These microscale natural cracks are typically sealed and cannot contribute to reservoir storage or enhance permeability. Our literature review yielded no evidence of widespread open natural microcracks. Although there are several open microcracks in core samples, they are likely induced by drilling or core removal and handling. Microcracks generally have only a slight effect on the macroscale seepage flow.[17] In the research on the influence that the evolution of microscale fractures has on the seepage, driven force, and strength of the shale, which affect the distribution of the macro-induced fractures, there are fewer studies on the influence of crack on the seepage flow in this scale according to our literature survey. Microcracks are generally treated as micropores in the study of seepage flow. However, natural microcracks with different geometry, orientation, and spacing parameter combinations weaken the rock integrity; they may be reactivated and change the propagation of induced fractures during hydraulic fracture treatments. Therefore, the natural microcracks actually have a non-negligible impact on the fracturing process, even if the impact is smaller than that of macronatural fractures. Thus, all natural cracks, including microcracks and large potentially open fractures, must be considered when predicting supercritical CO_2 fracturing behavior.

Numerical modeling is an important tool for engineers to predict the geometry of fracture networks and understand the fracturing mechanism. Many numerical studies have been conducted by using the commercially available codes PFC3D (particle flow code 3D), universal distinct element code (UDEC), and 3D distinct element code (3DEC) (Itasca Consulting Group, Inc, Minneapolis, Minnesota, USA). Hamidi et al simulated the initiation and propagation of hydraulically induced fractures with 3D distinct element code.[18] Zou et al presented a 3D distinct element method (DEM)-based fracturing model to investigate the mechanism of HFN propagation in naturally fractured shale formations.[19] Zhang et al developed a displacement discontinuity method (DDM)-based numerical model to simulate a fluid-rock coupling system.[20] Nagel et al used continuum and

discrete element modeling approaches to simulate the geomechanical process and investigate the complex nature of the coupled interactions between a propagating hydraulic fracture and the existing natural fractures.[21] Ju et al investigated the processes of the initiation and the propagation of cracks in a heterogeneous material based on the continuum-based discrete element method (CDEM) algorithm; the results indicated that material heterogeneity has considerable effect on crack initiation, but that crack propagation is controlled primarily by the geostress ratio.[22,23]Duan,Kwok, and Pierce proposed a numerical approach to modeling the mechanical behaviors of inherently anisotropic rocks by using the bonded particle model (BPM).[24] The research showed that the BPM approach can generally capture the brittle failure process of anisotropic rock under uniaxial compression. Samimi and Pak developed an element-free Galerkin mesh-less method for the numerical modeling of hydraulic fracture propagation.[25] Settgast et al proposed a fully coupled finite element/finite volume approach, which is capable of modeling large-scale problems that involve hydraulically driven fractures in 3 dimensions.[26]

The overall material response of rock is very complicated, and its anisotropy is governed mainly by micromechanisms such as the formation, growth, and eventual interaction of microcracks. The microstructure controls many of these micromechanisms, which are difficult to characterize within the framework of existing continuum theories. In the traditional continuous fracturing models, the mechanical properties of rock are input as macroscopic quantities. These models neglect the microcracks and discontinuity of rock, which is an important factor influencing the geometric structure of the induced fractures. To predict the geometric distribution of the induced fractures and investigate the impact of natural microcracks on the fracturing process, we simulate the supercritical CO_2 fracturing with BPM in this paper. The BPM approximates rock as a cemented granular material and provides a synthetic material that can be used to test hypotheses about how the microstructure affects the macroscopic behavior. There is much disorder in the BPM, including locked-in stresses produced during material genesis, grain deformability, and strength and the cement grain size, grain packing, and degree of cementation (ie, how much of the intergrain space is filled with cement). All of these items influence the mechanical behavior and characterize the anisotropy of rock. Because the rock is modeled at the microscale in PFC3D, investigation of the microfracturing and microdamage of the rock is feasible and effective. Using this method, we investigate the effect of the original natural microcracks on the induced fracture network distribution and analyze the influence of the horizontal stresses of an unconventional shale reservoir on the complex fracture network distribution. The numerical results indicate that the mechanical properties of the rock are closely related to the microdamage and that the natural microcracks must be considered to predict the geometric distribution of the induced fractures.

2 | BONDED PARTICLE MODEL APPROACH FOR ROCK

2.1 | Numerical model and physical parameters

To simulate and analyze the supercritical CO_2 fracturing characteristics of laboratory-scale shale samples, a 3D numerical model in the *X-Y-Z* coordinate system is established based on a BPM approach utilizing PFC3D[27]; the preexisting in situ stresses (S_H is the maximum horizontal principal stress, S_h is the minimum horizontal principal stress, and S_v is the vertical stress) are applied to the model as stress boundary conditions, as shown in Figure 1A. Because of the need to study the

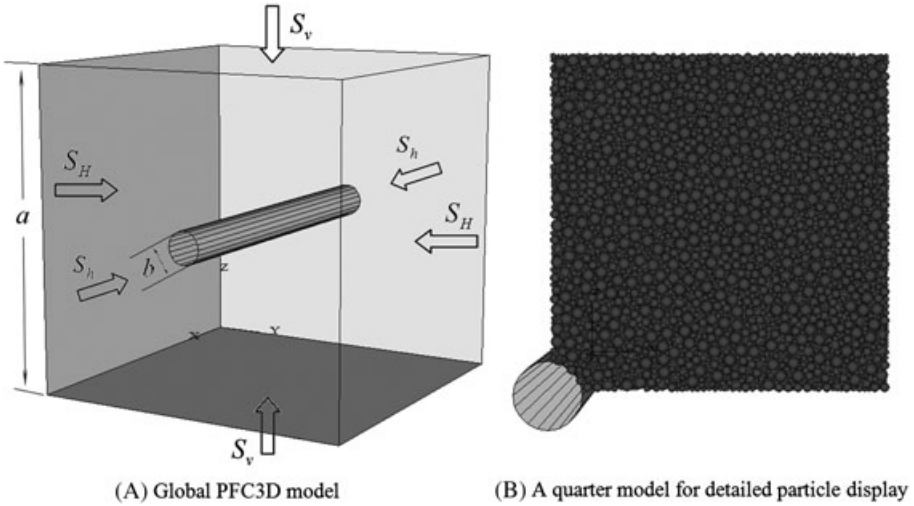

FIGURE 1 Global particle flow code 3D (PFC3D) model with in situ stresses and local enlargement for detailed particle display. S_H, S_h, S_v represent the maximum horizontal principal stress, the minimum horizontal principal stress, and the vertical stress, respectively

evolution of cracks at the microscopic scale, the particle size must also be in the micrometer scale. If the specimen is too large, numerical calculation will require a very long time. Thus, each side length a of the PFC3D model is set to 100 mm, where the diameter b of a borehole is 10 mm to match the size of the whole specimen, ie, one-tenth the size of a, to reduce the stress concentration effect of the in situ stress application, and the borehole axis is consistently perpendicular to the outer plane of the model.

Considering the simplification and taking full advantage of the symmetry of the model, the local quarter model shown in Figure 1B was adapted. Furthermore, based on the symmetric boundary conditions of the model, the Y-displacements on the left boundary and the Z-displacements on the lower boundary are set to 0.

To provide parameters for the numerical modeling of supercritical CO_2 fracturing, a few shale specimens that were sampled from the Longmaxi Formation in the Sichuan Basin in the southwest of China[28] were tested. The values of mechanical properties are listed in Table 1.

A numerical intact shale specimen was discretized into many small particles. In the process of generating the sample, an assembly consisting of larger particles is first built, and then the contact force of each particle is tested; these particles are deleted if the maximum contact force of a particle is less than one-tenth the average contact force of the entire sample. Smaller particles are then inserted in this porous sample, and the particles whose contact forces are sufficiently small are deleted according to the same rule. This process continues until a sample with sufficiently low porosity is created. The particle size of the final model followed a distribution ranging from 0.05 to 1.0 mm.

Two bonding models are supported in PFC3D: a contact-bond model and a parallel-bond model. Both bonds can be envisioned as a kind of glue joining the 2 particles. The contact-bond glue is of a vanishingly small size that acts only at the contact point, whereas the parallel-bond glue is of a finite size that acts over a circular cross section lying between the particles. The contact bond can only transmit a force, whereas the parallel bond can transmit both a force and a moment. The parallel-bond model is widely used to model rock.[29-31] As explained by Cho et al[32]: "The parallel bond model is a more realistic bond model for rock-like materials whereby the bonds may break in either tension or shearing with an associated reduction in stiffness." Thus, parallel bonding was selected as the type of bonding among microscale particles (the parallel bonds of the PFC model are illustrated in Figure 2).

There is an additional step in the modeling process that is not required when employing other continuum-type methods. The macroscopic mechanical parameters cannot be directly specified in the model established by PFC3D. The solid rock is represented as an assembly of particles bonded to one another at their contacts, PFC synthesizes macroscale material behavior from the interactions of microscale particles, and the macroscopic constitutive relation is controlled by the microparameters. Only the macromechanical properties of the specimen listed in Table 1 are known; the input properties of the microscopic constituents that must be specified in the numerical model are still not known.

The procedure to set the stiffness of the particles and parallel bonds as following the relationship between macroscopic and microscopic moduli is given as[27]

$$E = \frac{E_c}{\zeta} + \frac{\overline{E}_c}{\overline{\zeta}} \tag{1}$$

where E is the macroscopic modulus, E_c is the contact Young modulus caused by the particle-particle contacts, and $\overline{E}_c$ represent the Young modulus caused by each parallel bond. ζ and $\overline{\zeta}$ are the ratios of micromodulus to macromodulus contribution for the particle-particle contacts and the parallel bonds, respectively. These ratios can be estimated for a given particle system in accordance with the following procedures: (i) assign $\overline{E}_c = 0$ and measure the modulus to obtain an estimate of ζ and (ii) assign $E_c = 0$ and measure the modulus to obtain an estimate of $\overline{\zeta}$.

The relationship between normal and shear stiffnesses of particles and the contact Young modulus E_c at a single contact is given as[27]

$$k_n = k_s = 2\widetilde{R}E_c \tag{2}$$

TABLE 1 Mechanical properties of the shale of the Longmaxi Formation in the Sichuan Basin

Density (g cm^{-3})	Uniaxial Compressive Strength (MPa)	Tensile Strength (MPa)	Elastic Modulus (GPa)	Poisson Ratio
2.6	70	3.2	25	0.27

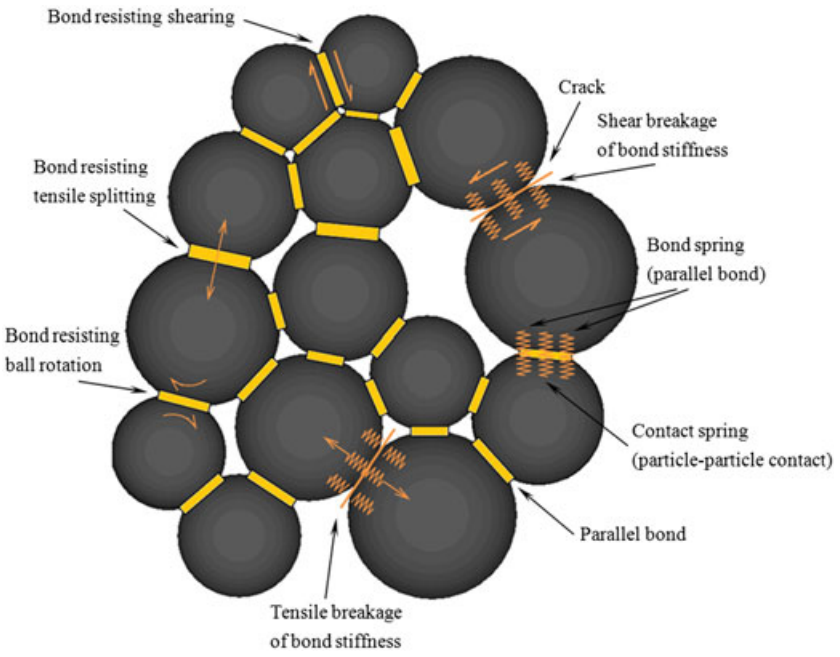

FIGURE 2 Illustration of the parallel bonds of the particle flow code (PFC) model. Parallel bonds establish an elastic interaction between particles that act in parallel with the contact constitutive model. When parallel bonds break, the particle-particle contact spring still works [Colour figure can be viewed at wileyonlinelibrary.com]

$$\widetilde{R} = \frac{R^{\mathrm{A}} + R^{\mathrm{B}}}{2} \tag{3}$$

where k_{n} and k_{s} represent the normal and shear contact stiffnesses, respectively, and the superscripts A and B represent the 2 contacting particles. For the linear contact model, the contact stiffnesses $k_{\mathrm{n}}, k_{\mathrm{s}}$ are computed, assuming that the stiffnesses of the 2 contacting particles act in series such that

$$k_{\mathrm{n}} = \frac{k_{\mathrm{n}}^{\mathrm{A}} k_{\mathrm{n}}^{\mathrm{B}}}{k_{\mathrm{n}}^{\mathrm{A}} + k_{\mathrm{n}}^{\mathrm{B}}} \tag{4}$$

$$k_{\mathrm{s}} = \frac{k_{\mathrm{s}}^{\mathrm{A}} k_{\mathrm{s}}^{\mathrm{B}}}{k_{\mathrm{s}}^{\mathrm{A}} + k_{\mathrm{s}}^{\mathrm{B}}} \tag{5}$$

The relationship between normal and shear stiffnesses of parallel bond $\overline{k}_{\mathrm{n}}$, $\overline{k}_{\mathrm{s}}$ and the Young modulus $\overline{E}_{\mathrm{c}}$ is given as[27]

$$\overline{k}_{\mathrm{n}} = \frac{\overline{E}_{\mathrm{c}}}{2\widetilde{R}} \tag{6}$$

$$\overline{k}_{\mathrm{s}} = \frac{3\overline{R}^2 \cdot \overline{E}_{\mathrm{c}}}{8\widetilde{R}^3} \tag{7}$$

where $\overline{R}$ is bond radius (as shown in Figure 3) that is set by specifying $\overline{\lambda}$, $\overline{R} = \overline{\lambda} \min\left(R^{\mathrm{A}}, R^{\mathrm{B}}\right)$, and $\overline{\lambda}$ is a parameter of a parallel bond that can be subjectively specified in PFC3D.

The value of the macroscopic Poisson ratio is related to the ratios of normal to shear stiffness $k_{\mathrm{n}}/k_{\mathrm{s}}$ and $\overline{k}_{\mathrm{n}}/\overline{k}_{\mathrm{s}}$, which can be determined to achieve the actual parameters through adjusting $k_{\mathrm{n}}/k_{\mathrm{s}}$ and $\overline{k}_{\mathrm{n}}/\overline{k}_{\mathrm{s}}$.

For the matching strength parameters, the proposed method is as follows: The proposed modeling process is divided into several steps. In each step, smaller particles are inserted into the existing porous sample. New contacts are formed when the

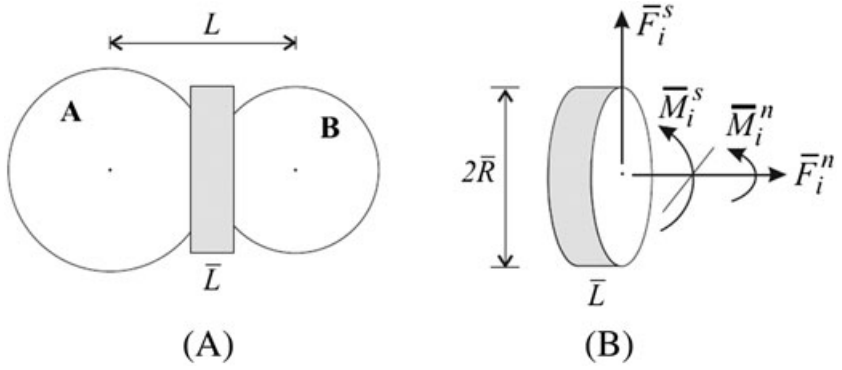

FIGURE 3 A, parallel-bond idealization and B, forces carried in the 3D bond material, where $\bar{F}_i^n$, $\bar{F}_i^s$, $\bar{M}_i^s$, and $\bar{M}_i^n$ represent the normal force, shear force, bending moment, and torsional moment, respectively

smaller particles are added; thus, new microparameters of the deformation and strength must be specified for these new contacts, such as the bond stiffness and bond strengths. These microparameters of newly specified stiffness and strength each step can be divided into several groups. The values of each group were gradually decreased. First, let the uniaxial compressive strength (UCS) of the numerical sample reach the desired value. At this time, the tensile strength is generally not matched. Then, the tensile strength is matched by adjusting the decrement between the microparameters formed in each step in every group. When the tensile strength is matched, the UCS may have changed, again resulting in a mismatch. Second, all microstrength parameters are adjusted proportionally to match the UCS again. It is necessary to perform several iterations of the first and second steps to match the UCS and tensile strength. Specific microparameters of the BPM are chosen if the elastic modulus, Poisson ratio, tensile strength, and UCS have the same values, as shown in Table 1.

Actually, shale exhibits highly anisotropic material behavior. Our model just ensures that the macroscopic mechanical properties are in agreement with Table 1. Because the focus of our study was not the effect of shale anisotropy on induced fracture geometry, our model did not fully reproduce the exact behaviors of all types of anisotropic rocks, such as in these anisotropy ratios: $K_{1,UCS}$, $K_{2,UCS}$, $K_{1,E}$, and $K_{2,E}$, as defined in the literature.[24] Of course, anisotropy of shale has influence on induced fracture geometry; we will investigate these effects in our future studies.

2.2 | Rock deformation and particle motion

Based on the BPM approach, rock deformation is composed of the motion of a number of microparticles, which motion is calculated by using law of motion. The forces applied to each particle include the contact force among the particles, gravity force, buoyancy force, driving force of the fluid, and moment. At each step, the contact of each particle is updated according to the relative motion position constitutive law and computed by using the force-displacement law. By the time-stepping algorithm, calculation cycle in PFC3D will update particle and wall positions and set of contacts with law of motion and force-displacement law as shown in Figure 4. The parallel bonding technique is adapted in the proposed model in this paper.

In the simulation, the relative motion between bonded particles causes force and moment within the shale sample because of the parallel-bond stiffness. The parallel-bond model describes the constitutive behavior of a finite-sized piece of cementitious material deposited between 2 particles (see Figure 5). The total force and moment associated with the parallel bond can be resolved into normal and shear components. These forces and moments act on the 2 bonded particles and produce the

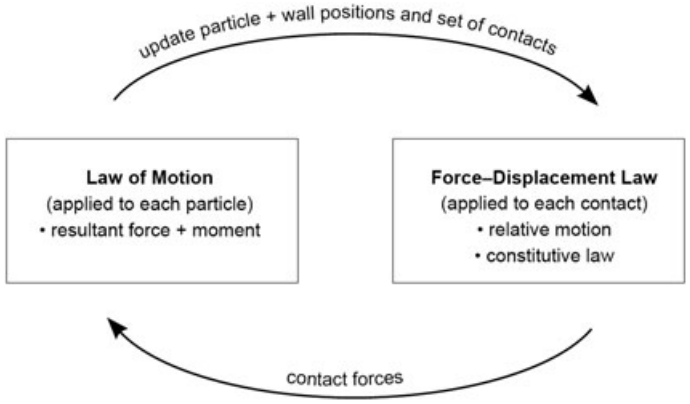

FIGURE 4 Calculation cycle in particle flow code 3D (PFC3D)

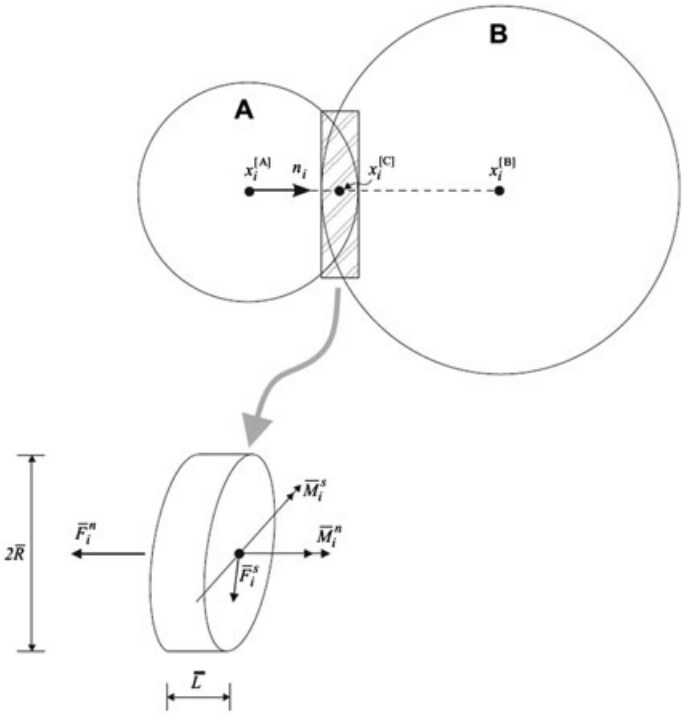

FIGURE 5 Parallel bond depicted as a cylinder of cementitious material. $\overline{F}_i^n$, $\overline{F}_i^s$, $\overline{M}_i^s$, and $\overline{M}_i^n$ represent the normal force, shear force, bending moment, and torsional moment, respectively

corresponding normal stress, and shear stress within the bond material and maximum normal and shear stresses appear at the bond periphery. The maximum tensile and shear stresses are calculated (via beam theory) as[27]

$$\sigma_{\max} = \frac{-\overline{F}_i^n}{A} + \frac{\left|\overline{M}_i^s\right|}{I}\overline{R} \tag{8}$$

$$\tau_{\max} = \frac{\left|\overline{F}_i^s\right|}{A} + \frac{\left|\overline{M}_i^n\right|}{J}\overline{R} \tag{9}$$

where A, I, and J are the area, moment of inertia, and polar moment of inertia of the circular section, respectively. If the maximum tensile stress exceeds the normal strength, or the maximum shear stress exceeds the shear strength, then the parallel bond breaks and there is a fracture in the rock.

2.3 | Fluid flow algorithms

The flow of the fracturing fluid in the BPM is considered as a fluid flow in porous media; the fracturing fluid is filled with rock pores, which have saturated seepage, and the fracturing fluid is an incompressible fluid with constant density. The Navier-Stokes equation for the solid fluid 2-phase flow system per unit volume is given by Equation 10.[27] The fluid pressure field and velocity field are obtained by solving the continuity equations and Navier-Stokes equations numerically.

$$\frac{\partial(n\mathbf{u})}{\partial t} = -(\nabla\cdot n\mathbf{u}\mathbf{u}) - \frac{n}{\rho_f}\nabla p - \frac{n}{\rho_f}\nabla\cdot\boldsymbol{\tau} + n\mathbf{g} + \frac{\mathbf{f_{int}}}{\rho_f} \tag{10}$$

where n is the porosity, $\mathbf{u}$ is the fluid velocity vector, ρ_f is the density of the fracturing fluid, $\boldsymbol{\tau}$ is the viscous stress tensor, $\mathbf{g}$ is the gravitational acceleration, and $\mathbf{f_{int}}$ is the interaction force per unit volume between the particles and fluid.

The porosity n is defined at the center of fluid cells; the definition of porosity n is given by[27]

$$n = 1 - \frac{1}{\Delta V}\frac{\pi}{6}\sum_{i=1}^{n_p} d_{pi}^3 \tag{11}$$

where ΔV is the volume of a fluid cell, n_p is the number of particles in the fluid cell, and d_{pi} is the particle diameter.

Supercritical CO_2 fluids have the characteristics of high density, similar to liquid, and ultra-low viscosity, similar to gas. In the proposed numerical simulation of fracturing, the special effects of physical and mechanical properties of supercritical CO_2 on fracturing are focused on when the temperature is above 32°C; the pressure is approximately 10 to 16 MPPa. Under these conditions, the density of supercritical CO_2 changes very low; that is, it is almost incompressible.

2.4 | Rock deformation-fluid flow coupling

In the calculation of interaction between the particles and fracturing fluid, driving forces from the fluid flow are applied to the particles as body forces. The calculating formula is given by[27]

$$f_{\mathrm{d}_{\mathrm{i}}} = -\frac{\nabla p_{\mathrm{j}}}{1-n}\frac{\pi}{6} d_{\mathrm{pi}}^3 \tag{12}$$

where d_{pi} is the particle diameter; p is the pressure; $i = 1, \ldots, n_{\mathrm{p}}$ represent a particle; and $j = x, y, z$ represent the x, y, or z component of the driving force.

These forces are also added to the fluid equations and cause a change in momentum, as reflected by the change in the pressure gradient in the flow direction.

Mechanical calculations and fluid calculations are carried out alternately to realize the coupling calculation of fluid and particles. In the mechanical calculation (distinct element method), the interaction forces on particles are added as external body forces, and then the law of motion and force-displacement law are performed. If the time of the mechanical calculation exceeds the predicted time for the next fluid step, then the fluid calculation is executed. In general, the time step for the mechanical calculation is considerably smaller than that for the fluid calculation; that is, the driving forces applied to the particles are temporarily constant during several mechanical calculation cycles until the next fluid calculation is conducted.

2.5 | Natural microcrack generation technology

In the BPM, the intact rock is represented by an assembly of separate particles bonded together, where the damage process is represented by the breakage of these bonds. Traditionally, fractures are modeled as an interface between 2 opposite blocks along which the particles are initially unbounded[33] or simply deleting the particles from the fracture space for this type of fracture with a certain width.[34] In this study, fractures are modeled by the method of deleting the bonds between particles.

A flat ellipsoid is used to produce a crack cluster composed of many microcracks (as shown in Figure 6). The location, azimuth angle, and size of the ellipsoid are generated randomly, so the ellipsoid can be very small or relatively large. It can represent a macroscopic crack when it is large, or it can be merely a collection of several microscopic cracks when it is very small. The central coordinates of the flat ellipsoid (x_0, y_0, z_0) are 3 random numbers in the range of 0 to 100 mm and follow a uniform distribution. The angle position is expressed by the 3 angles (α, β, γ) by which the ellipsoid is rotated around the X-axis, Y-axis, and Z-axis, respectively. The parameters (α, β, γ) are also 3 random angles that obey a uniform distribution with a range of 0 to

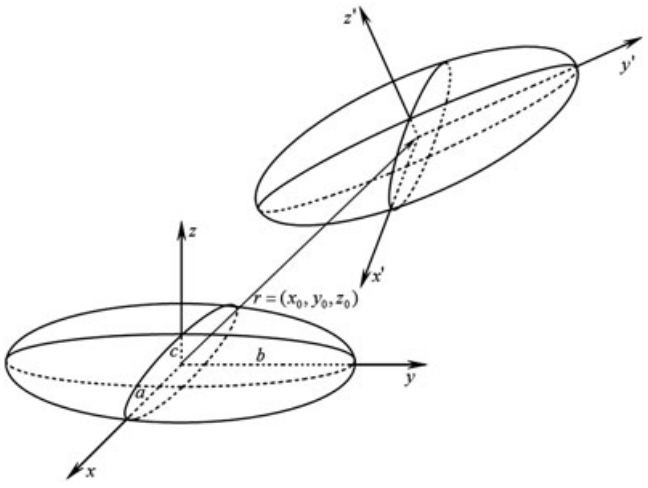

FIGURE 6 Flat ellipsoid with random location and azimuth angle

180°. The 3 principal axes of the ellipsoid (a, b, c) are randomly distributed between 0 and 1 mm, where the length of c is considerably smaller than the other 2 principal axis lengths of a and b. When the parallel bond between the particles is located within the flat ellipsoid, the bond is deleted to simulate the microcrack. In this manner, there may be 3 cases: (1) there exist parallel bonds in the ellipsoid, but no particles are completely located inside the ellipsoid; (2) it is possible that several particles are completely located inside the ellipsoid; and (3) no parallel bonds exist in the ellipsoid. For cases 1 and 2, we simply delete the parallel bonds and do not delete any microparticles in the flat ellipsoid. The purpose of doing so is to better simulate the closure of the natural microfractures, which have no effect on the seepage flow directly and only weaken the integrity of the rock. Case 3 represents the failure to generate a fracture, and there is no microcrack accumulated in the total number in the Statistics.

3 | BREAKDOWN PRESSURE COMPUTATION

3.1 | Breakdown pressure of hydraulic and supercritical CO_2 fracturing

The breakdown pressure is tested based on the numerical sample and compared with the theoretical results to verify the proposed model. There are 2 control methods in the testing process when carrying out the fracturing simulation: (i) control the fluid flow speed when injecting fracturing fluid into the borehole and (ii) control the pressure in the injection borehole. Under the first control method, fluid flow speed to the injection borehole is designated and the pressure changes with the flow rate. The pressure decreases when the sample breaks down. Under the second control method, the pressure is designated and the injection speed is a function of pressure. The pressure control method is used in our simulation. The injection pressure increases linearly with time when fluid is injected in the model, and the cumulative number of parallel-bond breaking events is recorded with increasing pressure; the corresponding pressure curve is shown in Figure 7. A sudden dramatic increase in the cumulative number of parallel-bond breakages indicates that the breakdown pressure should be this specific pressure; the distribution of the broken parallel-bond locations (as shown in Figure 8) indicates that most of them are concentrated in the periphery of the borehole.

For simplicity, we assume that the minimum horizontal stress S_h and maximum horizontal stress S_H are equal in the verification model. The breakdown pressures of 2 different viscous fracturing fluids under 6 different horizontal stresses are simulated, and the numerical results are shown in Table 2.

3.2 | Numerical model benchmark

The breakdown pressure for the impermeable case is given as[35]

$$P_b = 3S_h - S_H - p_f + T, \tag{13}$$

where T is the rock tensile strength, p_f is the pressure in the fracture or in the pores where the fracture is formed, S_H is the major horizontal stress, and S_h is the minor horizontal stress.

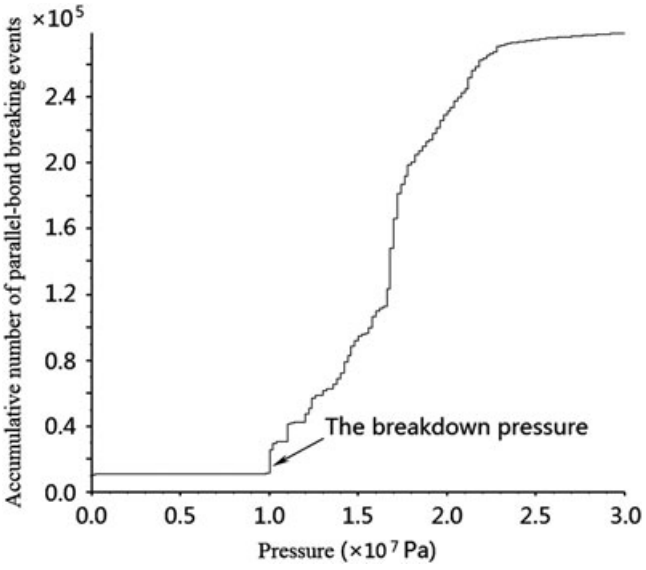

FIGURE 7 Cumulative number of parallel-bond breaking events versus pressure

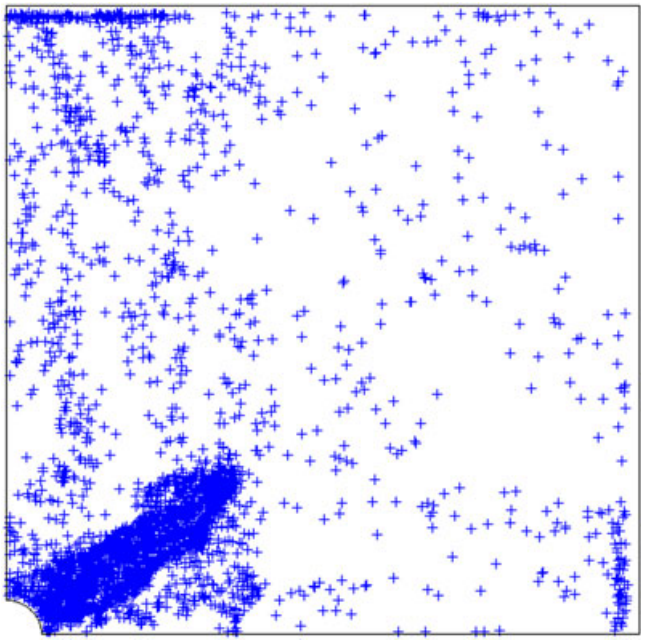

FIGURE 8 Distribution of the broken parallel-bond locations (2D side view). Note: The position of broken parallel bond is actually 3-dimensional spatial distribution. The reason for displaying with 2-dimensional side view is because the density and distribution of microcracks are better identified in the 2-dimensional side view. On the contrary, the 3-dimensional view is just like a mess [Colour figure can be viewed at wileyonlinelibrary.com]

If it is assumed to be fully permeable and the pressurization rate is sufficiently low to ensure steady-state conditions during pumping, then the relationship between the breakdown pressure P_b and horizontal stress is as follows[35]:

$$P_b = \frac{3S_h - S_H - \alpha(1-2\mu)/(1-\mu)p_f + T}{2-\alpha(1-2\mu)/(1-\mu)}, \quad 0 \le \alpha \le 1 \tag{14}$$

where α is the poroelastic coefficient and μ is Poisson ratio.

The poroelastic coefficient α is defined as[35]

$$\alpha = 1 - \frac{K_r}{K_m} \tag{15}$$

where K_r is the bulk modulus of porous dry rock and K_m is the bulk modulus of skeleton material.

For our numerical sample, particle assembly represents porous rock and every single particle is considered skeleton material. Thus, the bulk modulus K_r of porous dry rock can be calculated based on the whole sample and the bulk modulus K_m of the skeleton material is calculated based on the stiffness of the particle. The value of poroelastic coefficient of our numerical sample is 0.89. We calculated the breakdown pressure of 6 different horizontal stresses for the fully permeable case. The value of the pressure p_f for the fully permeable case in the theoretical calculation is obtained by using the pressure of the fluid cell at the crack initiation location in the numerical model.

The comparisons between the analytical solutions and numerical simulation results are shown in Figure 9. The result is almost in agreement with the theory on the overall trend. The numerical results agree with the analytical solutions well when the fracturing fluid is supercritical carbon dioxide (viscosity = 0.02 m Pa s). However, the error is slightly larger when the fracturing fluid is common fracturing fluid (viscosity = 100 m Pa s). The maximum error is approximately 18%, possibly because the breakdown pressure formula 17 from *Petroleum Related Rock Mechanics* is under the condition that the pressurization rate

TABLE 2 Numerical results of the breakdown pressure (MPa)

Viscosity (m Pa s)	Horizontal Stress (MPa)					
	10	11	12	13	14	15
0.02	9.17	10.33	11.07	11.69	13.15	13.82
100	11.41	12.27	12.46	14.09	14.65	15.81

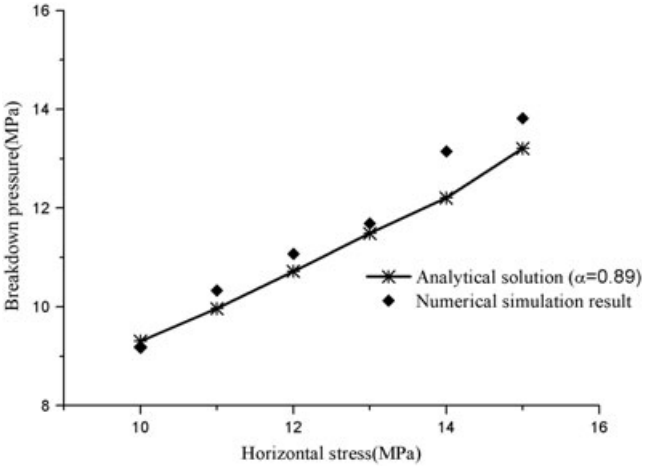

FIGURE 9 Comparison of numerical results and analytical solutions. The analytical solutions are based on the assumption that the pressurization rate is sufficiently low to ensure that steady-state conditions during pumping and the pressurization rate in the numerical simulation did not exactly match this condition. Therefore, the actual maximum error may be smaller

is sufficiently low to ensure steady-state conditions during pumping. Our verification process did not exactly match this condition. Further, a larger viscosity leads to slightly larger error. To assess the trend of the breakdown pressure influenced by the pressurization rate, numerical simulations of hydraulic fracturing under different pressurization rates were carried out (as shown in Figure 10). The breakdown pressure exhibited an overall decreasing trend with decreasing pressurization rate.

In fact, the pressurization rate cannot be infinitesimal in practical engineering, so the simulated value by PFC3D may even be closer to reality than the analytical value. In fact, the possibility of using the BPM to simulate fluid flow in rock materials has been identified in some studies.[36,37] Of course, the simulation of hydraulic fracturing is related not only to fluid flow but also to crack initiation and crack propagation. Our literature survey[38-40] and the above analysis indicate that the BPM is feasible for modeling the fracturing process to an acceptable degree.

4 | DISTRIBUTION UNIFORMITY INDEX ANALYSIS OF THE INDUCED FRACTURE NETWORK DISTRIBUTION

In the fracturing process of the 3-dimensional BPM, the event of parallel bond breakage represents the induced-fracture propagation. We can study the induced-fracture network distribution through the statistical analysis of the number and locations of the broken parallel bonds. The extension of the induced fracture is longer when there are a greater number of broken parallel

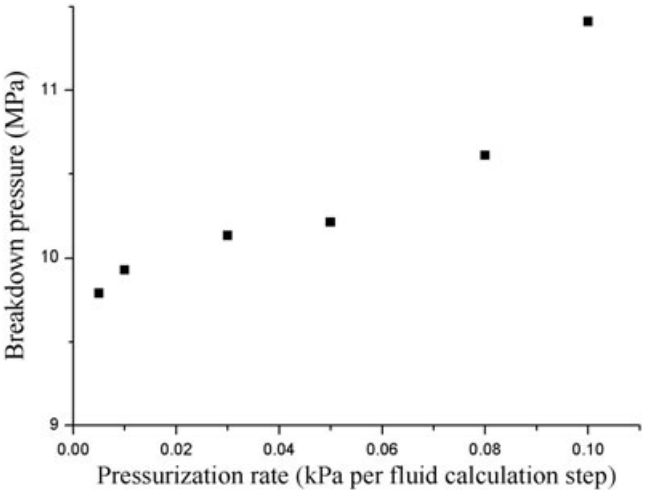

FIGURE 10 The breakdown pressure with different pressurization rate (the abscissa represents the rate of pressure increases every fluid calculation step, such that the value 0.1 means that pressure in the injection borehole increases by 0.1 kPa every fluid calculation step). As can be seen from the figure, breakdown pressure presented an overall trend of decrease with decreasing pressurization rate

bonds. In addition, the concentrated distribution and dispersive distribution of fractures can also produce different gas recovery efficiencies in the actual fracturing engineering. In this paper, a uniformity index is defined, and the distribution of induced fractures is analyzed through calculation of the total number and uniformity index of parallel bond breaking events.

In the fracturing simulation, the spatial position information of every broken parallel bond is recorded. When the simulation is finished, the distribution uniformity index (DUI) is calculated according to the following method. The model sample is divided into 8^n ($n=0,\ 1,\ 2,\ldots$) small cubes (as shown in Figure 11). The cube for each side is $100/2^n$ mm. The position of each broken parallel bond must be located in one of the 8^n cubes. In these cubes, the number of cubes that include a broken parallel bond is recorded as $g(n)$.

$$f(n) = \frac{g(n)}{8^n},\ n = 0,\quad 1,\quad 2,\ldots \tag{16}$$

The function $f(n)$ is plotted in the coordinate system in Figure 12; the ratio of the area surrounded by the curve $f(n)$ and curve $f_0(n)$ divided by the area surrounded by the curve $f_1(n)$ and curve $f_0(n)$ is defined as the DUI, where the functions $f_0(n)$ and $f_1(n)$ are as follows:

$$f_0(n) = \frac{1}{8^n},\ f_1(n) = 1 \tag{17}$$

From the definition of the DUI, when the distribution of the cracks is highly concentrated, even if the cube is divided into small segments, all of the cracks are always located in a cube in this extreme case:

$$f(n) = f_0(n) = \frac{1}{8^n} \tag{18}$$

DUI = 0.

Another extreme case is when the crack distribution is absolutely uniform; even if the cube is divided into small segments, all of the cubes always contain cracks, namely,

$$f(n) = f_1(n) = 1 \tag{19}$$

DUI = 1.

Theoretically, the cubic sample can be divided infinitely. However, in the calculation of this paper, the maximum of n is only 6. If the number n is too large, then the volume of the small cube may be smaller than the size of the microparticles, and then it is

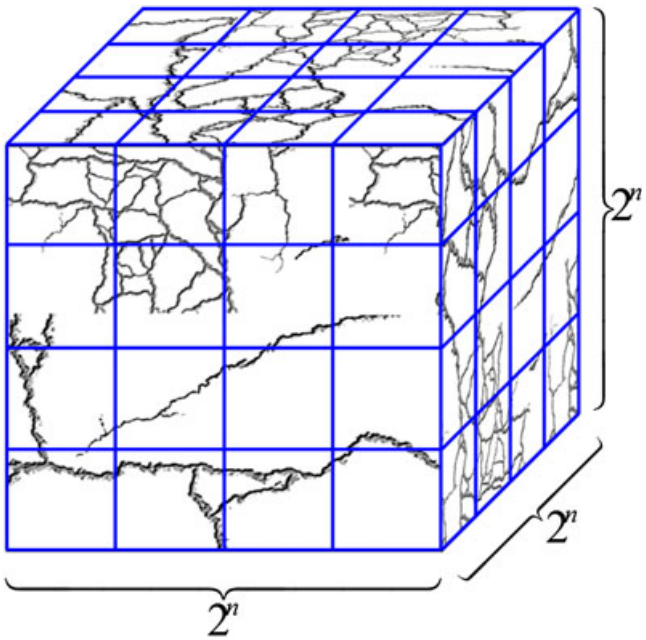

FIGURE 11 The cube is divided into 8^n parts ($n=2$ for illustration). Actually, the distribution uniformity index (DUI) of the spatial position of broken parallel bonds is calculated in this paper, but the spatial position information is discrete; to facilitate the understanding, the graph shows the division of a cube sample containing continuous fracture network [Colour figure can be viewed at wileyonlinelibrary.com]

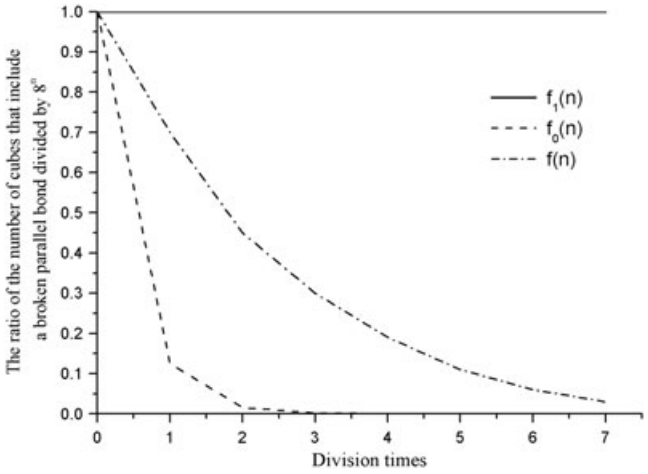

FIGURE 12 Distribution uniformity index (DUI) calculated by the ratio of the areas surrounded by $f(n)$, $f_0(n)$ curves and $f_1(n)$, $f_0(n)$ curves $f(n)$ is an arbitrary curve just for illustration)

of no practical significance to continue to divide the cube. In the calculation of the DUI, only the areas in front of the vertical line $n = 6$ are considered.

5 | EFFECT OF NATURAL MICROCRACKS ON THE INDUCED FRACTURE NETWORK DISTRIBUTION

A series of numerical simulations was performed by using the configuration shown in Figure 1 to investigate the effects of the natural microcrack distribution on the induced-fracture network distribution. Some of the other influential factors, such as the horizontal stress ratio, are also considered in the model.

5.1 | Number of natural microcracks

A good understanding of the mechanical properties of unintact rock with microcracks is required before simulating a fracturing process in PFC3D. The macroproperties of the specimen are not known at the beginning of the simulation, and there is no explicit method to estimate them, only numerical tensile and compressive tests.

For the numerical experiments in this section, the elastic modulus, Poisson ratio, UCS, and tensile strength of 16 samples are tested, and the results are shown in Table 3 and Figures 13 and 14. Sample S0 did not delete any parallel bonds; other samples are generated by the random crack generation function (as described in section 2.5) based on sample S0. A total of 5 groups of samples containing microcracks were generated, with 3 samples in each group. The number of deleted parallel bonds was

TABLE 3 Mechanical properties of the samples by numerical calculation

Samples	Tensile Strength (MPa)	UCS (MPa)	Elastic Modulus (GPa)	Poisson Ratio	Samples	Tensile Strength (MPa)	UCS (MPa)	Elastic Modulus (GPa)	Poisson Ratio
S0	3.2	72.201	24.808	0.18	S3-2	1.142	49.861	23.565	0.18
S1-1	0.551	40.243	16.785	0.301	S3-3	1.019	50.967	24.726	0.125
S1-2	0.5891	40.831	19.278	0.322	S4-1	1.494	59.066	27.308	0.142
S1-3	0.495	40.103	18.035	0.278	S4-2	1.513	56.553	26.254	0.234
S2-1	0.836	45.878	21.904	0.162	S4-3	1.625	57.295	26.329	0.177
S2-2	0.883	45.997	21.797	0.297	S5-1	2.187	64.666	31.367	0.132
S2-3	0.788	46.718	21.803	0.221	S5-2	2.178	64.491	29.612	0.11
S3-1	1.358	51.149	25.061	0.15	S5-3	1.899	63.182	31.007	0.142

UCS indicates uniaxial compressive strength.

approximately equal between the same group samples, and the number of deleted parallel bonds was different among different groups. The total number of randomly deleted parallel bonds of each sample is shown in Table 4.

Figures 13 and 14 illustrate that the total number of randomly deleted parallel bonds in the sample has a significant impact on the elastic modulus, UCS, and tensile strength. With the increase of the total number of deleted parallel bonds, the elastic modulus, UCS, and tensile strength all exhibited a linear decrease, whereas the total number of deleted parallel bonds had no significant effect on Poisson ratio.

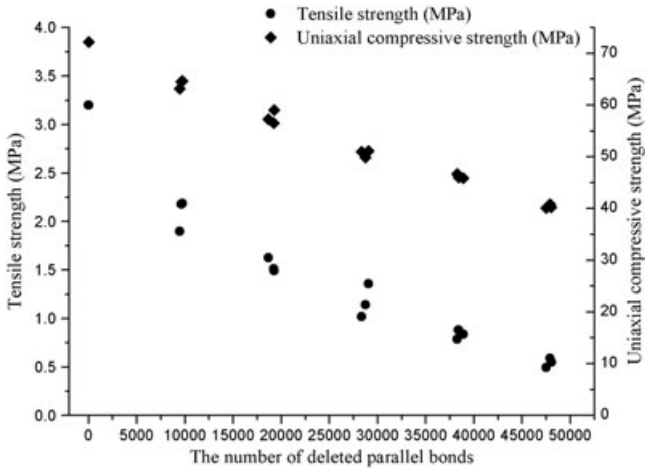

FIGURE 13 Tensile strength and uniaxial compressive strength (UCS) versus number of deleted parallel bonds

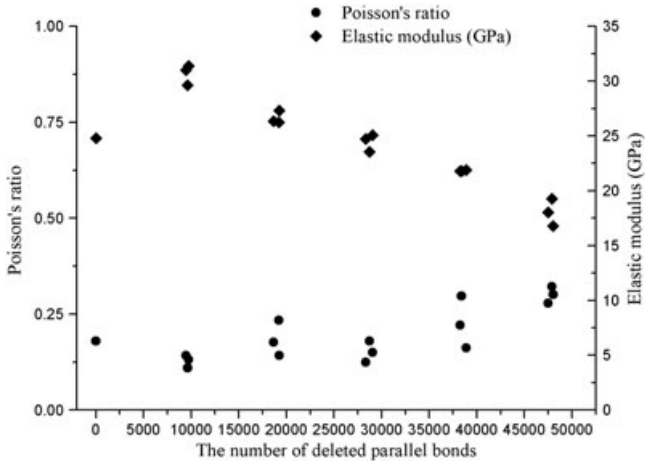

FIGURE 14 Elastic modulus and Poisson ratio versus number of deleted parallel bonds

TABLE 4 Total number of deleted parallel bonds of each sample

Samples	Number of Deleted Parallel Bonds	Samples	Number of Deleted Parallel Bonds
S0	0	S3-2	28,750
S1-1	48,028	S3-3	28,348
S1-2	47,882	S4-1	19,273
S1-3	47,486	S4-2	19,202
S2-1	38,907	S4-3	18,662
S2-2	38,394	S5-1	9,750
S2-3	38,237	S5-2	9,642
S3-1	29,039	S5-3	9,477

5.2 | Distribution uniformity index of natural microcracks

The elastic modulus, Poisson ratio, UCS, and tensile strength of the 12 samples are tested in this section, and numerical and experimental results are shown in Table 5 and Figures 15 and 16. The total number of deleted parallel bonds of each sample is equal, but the parameters in the random crack generation function (as described in section 2.5) are different, resulting in different DUIs of the generated microcracks (see Figure 17) to investigate the relationship between the mechanical properties of the sample and the DUI with the same total number of deleted parallel bonds.

TABLE 5 Mechanical properties of samples with different distribution uniformity indexes (DUIs)

DUI	Tensile Strength (MPa)	UCS (MPa)	Elastic Modulus (GPa)	Poisson Ratio	DUI	Tensile Strength (MPa)	UCS (MPa)	Elastic Modulus (GPa)	Poisson Ratio
0.4507	1.705	63.733	24.838	0.239	0.5517	2.488	65.43	18.85	0.256
0.4758	2.042	64.743	25.121	0.124	0.5608	2.373	63.561	18.283	0.232
0.4764	2.361	64.222	25.283	0.11	0.5625	2.383	64.341	19.052	0.266
0.5094	2.265	65.476	18.364	0.247	0.5716	2.436	64.268	18.728	0.244
0.5097	2.373	64.671	18.769	0.229	0.6095	2.554	65.608	18.283	0.241
0.5262	2.393	64.724	18.607	0.236	0.6394	2.631	65.952	18.566	0.244

UCS indicates uniaxial compressive strength.

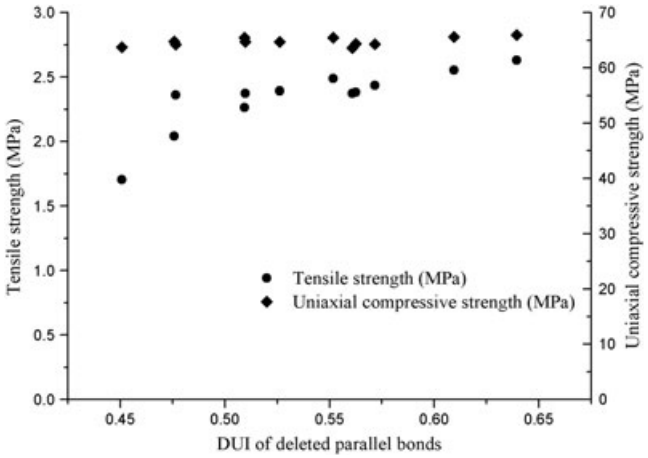

FIGURE 15 Tensile strength and uniaxial compressive strength (UCS) versus distribution uniformity index (DUI)

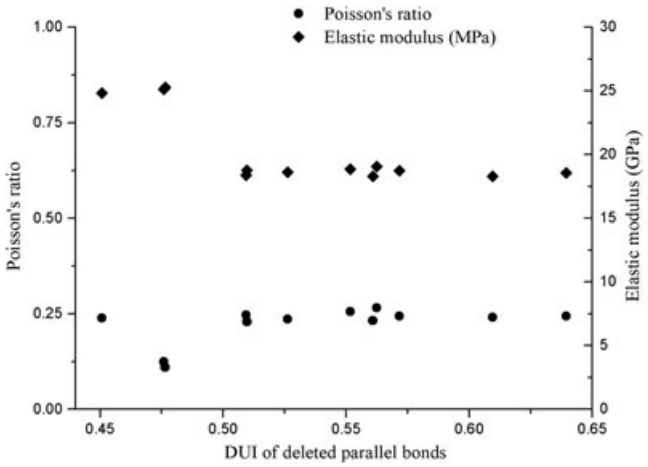

FIGURE 16 Elastic modulus and Poisson ratio versus distribution uniformity index (DUI)

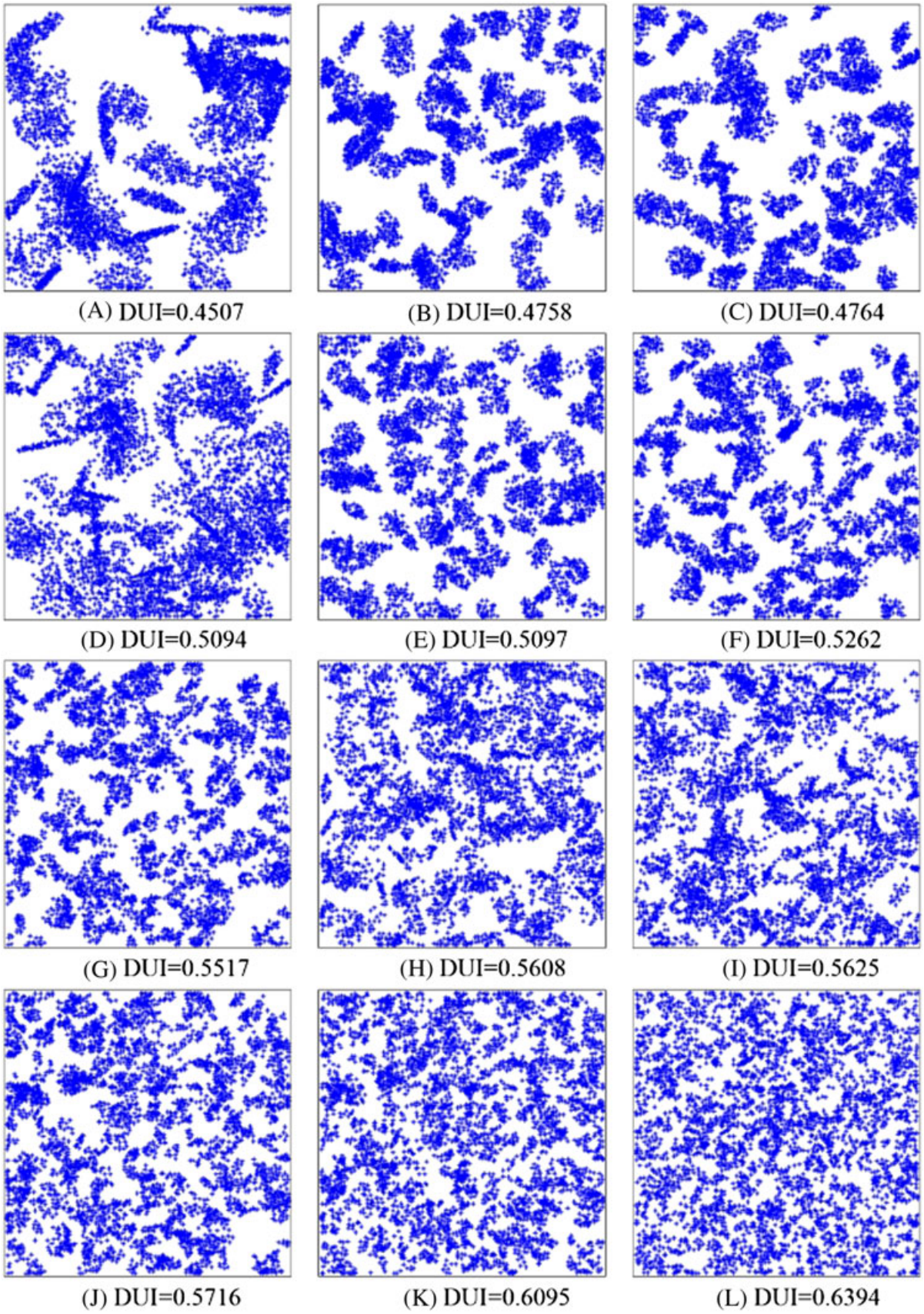

FIGURE 17 Distribution uniformity index (DUI) and distribution of the deleted parallel bonds of the samples (2D side views). Note: The model we built is 3-dimensional; 2-dimensional side views are used only for display because the density and distribution of microcracks are better identified in the 2-dimensional side view. On the contrary, the 3-dimensional view is just like a mess [Colour figure can be viewed at wileyonlinelibrary.com]

The mechanical properties of each sample obtained by the numerical experiments are sorted as shown in Figures 15 and 16. The DUI of the same number of random cracks has a significant impact on the tensile strength. With the same total number of cracks, the tensile strength increases with increases in the DUI. However, the DUI has no significant effect on Poisson ratio, the UCS, and/or the elastic modulus.

To understand how the initial natural microcracks affect the creation of the induced fracture network, we studied the cumulative number and DUI of the induced fracturing cracks for various DUIs of initial microcrack patterns. In the numerical experiments, the minimum horizontal stress S_h and maximum horizontal stress S_H are assumed to be 10 MPa and the fracturing processes of all samples were performed under 2 types of viscous fracturing fluid; one viscosity is set to 100 m Pa s to simulate the common hydraulic fracturing fluid, and another viscosity is set to 0.02 m Pa s to simulate the supercritical CO_2 fracturing fluid. From section 5.2, the total number and DUI of natural microcracks have a certain impact on the mechanical properties of the sample. In the numerical experiments of this section, the microparameters of the 12 samples are adjusted before the fracturing numerical experiments to eliminate this impact. The samples with different DUIs of natural microcracks after adjustment have the same mechanical properties as shown in Table 1. Then, the cumulative number and DUI of the induced fracturing cracks are calculated when the fracturing process runs 10,000 steps after the crack initiation of the model. The final numerical results of the fracturing simulation are shown in Tables 6 and 7.

Figures 18 and 19 illustrate that when the samples have different DUIs of randomly generated microcracks with the same total number of deleted parallel bonds, the cumulative number and DUI of the induced fracturing cracks are quite different after the fracturing process. The accumulative number and DUI increase with increases in the initial DUI. This type of increasing trend of the viscosity at 0.02 is more obvious than that of the viscosity at 100. Simulation results indicate that the cumulative number and distribution uniformity of the induced cracks significantly depend on the DUI of preexisting natural microcracks.

The above numerical results also illustrate that the distribution of induced cracks produced by the fracturing process is not the same even though the macromechanical parameters are the same. This result is mainly attributed to the different distribution of the initial microcracks and demonstrates that the elastic modulus, Poisson ratio, UCS, tensile strength, and other macroparameters of the sample alone cannot fundamentally predict the distribution characteristics of the induced cracks after fracturing, such as the DUI of the cracks.

TABLE 6 Numerical results of the distribution uniformity index (DUI) of induced fracturing cracks (viscosity = 0.02 m Pa s)

DUI of Initial Natural Microcracks	Cumulative Number of Induced Fracturing Cracks	DUI of Induced Fracturing Cracks	DUI of Initial Natural Microcracks	Cumulative Number of Induced Fracturing Cracks	DUI of Induced Fracturing Cracks
0.4507	13,769	0.3482	0.5517	17,971	0.4657
0.4758	11,553	0.3955	0.5608	19,694	0.5025
0.4764	14,247	0.4172	0.5625	22,008	0.5099
0.5094	15,118	0.4357	0.5716	23,782	0.5509
0.5097	16,717	0.4445	0.6095	27,509	0.5916
0.5262	18,038	0.4587	0.6394	30,160	0.6365

TABLE 7 Numerical results of the distribution uniformity index (DUI) of induced fracturing cracks (viscosity = 100 m Pa s)

DUI of Initial Natural Microcracks	Cumulative Number of Induced Fracturing Cracks	DUI of Induced Fracturing Cracks	DUI of Initial Natural Microcracks	Cumulative Number of Induced Fracturing Cracks	DUI of Induced Fracturing Cracks
0.4507	15,916	0.4027	0.5517	20,433	0.4074
0.4758	15,857	0.3561	0.5608	20,283	0.4322
0.4764	16,746	0.3718	0.5625	21,281	0.4235
0.5094	15,985	0.3989	0.5716	21,954	0.4436
0.5097	18,831	0.3959	0.6095	24,259	0.4475
0.5262	19,180	0.4028	0.6394	25,321	0.4559

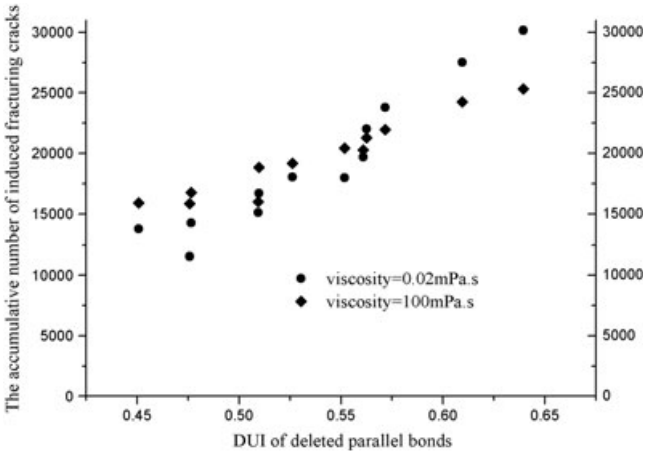

FIGURE 18 Accumulative number of induced fracturing cracks (viscosity = 0.02 and 100 m Pa s)

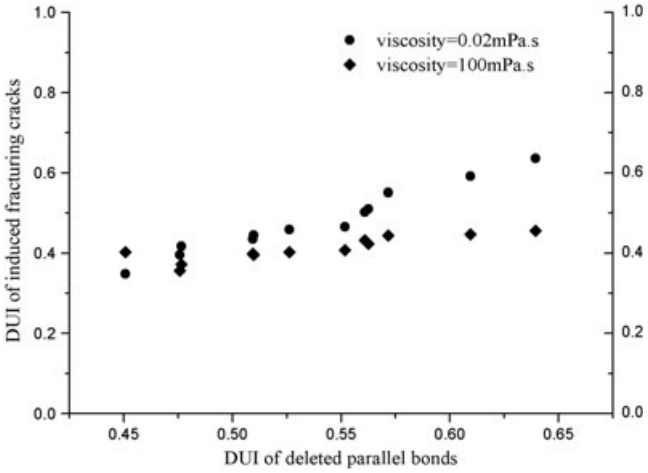

FIGURE 19 Distribution uniformity index (DUI) of induced fracturing cracks (viscosity = 0.02 and 100 m Pa s)

5.3 | Horizontal in situ stress ratio

In this section, we focus on the influence of the horizontal stress ratio on the relationship between the DUI of natural microcracks and the induced fracturing cracks. The fracturing simulation was carried out for 8 samples with different DUIs of initial microcracks under different horizontal stress ratios. The viscosity is set to 0.02 m Pa s in the numerical simulation. The cumulative number and DUI of the induced fracturing cracks were calculated at 10,000 steps after the crack initiation. The numerical results are shown in Tables 8–10 and Figures 20 and 21.

The DUI of the induced fracturing cracks increases with increases in the DUI of the initial microcracks when the horizontal stress ratio is relatively small. The correlation between the DUI of the induced fracturing cracks and that of the initial microcracks is not obvious when the horizontal stress ratio is larger, and the DUI of induced fracturing cracks can even decrease with the increase in the DUI of the initial microcracks. The DUI of induced fracturing cracks is relatively larger when the horizontal stress ratio is smaller if the other conditions are the same, such as the mechanical properties, DUI of the initial microcracks, and so on.

TABLE 8 Numerical results of the distribution uniformity index (DUI) of induced fracturing cracks (S_h = 10 MPa, S_H = 11 MPa)

DUI of initial natural microcracks	0.4507	0.4758	0.5097	0.5262	0.5517	0.5716	0.6095	0.6394
Cumulative number of induced fracturing cracks	14,782	15,612	17,697	18,046	17,999	20,147	23,125	24,187
DUI of induced fracturing cracks	0.3396	0.3869	0.4359	0.4501	0.4571	0.5422	0.5830	0.6278

TABLE 9 Numerical results of the distribution uniformity index (DUI) of induced fracturing cracks (S_h = 10 MPa, S_H = 13 MPa)

DUI of initial natural microcracks	0.4507	0.4758	0.5097	0.5262	0.5517	0.5716	0.6095	0.6394
Cumulative number of induced fracturing cracks	11,316	12,587	15,144	15,953	16,979	18,550	20,298	25,564
DUI of induced fracturing cracks	0.5200	0.4392	0.4775	0.4425	0.4258	0.4365	0.4822	0.4967

TABLE 10 Numerical results of the distribution uniformity index (DUI) of induced fracturing cracks (S_h = 10 MPa, S_H = 15 MPa)

DUI of initial natural microcracks	0.4507	0.4758	0.5097	0.5262	0.5517	0.5716	0.6095	0.6394
Cumulative number of induced fracturing cracks	12,897	11,907	12,543	14,559	16,638	19,566	18,858	20,370
DUI of induced fracturing cracks	0.5016	0.4207	0.4894	0.4313	0.4510	0.5224	0.4956	0.5646

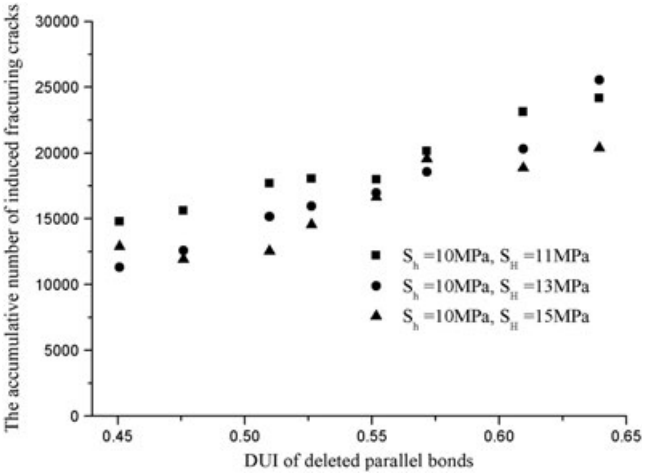

FIGURE 20 Cumulative number of induced fracturing cracks (horizontal stress ratio = 1.1, 1.3, and 1.5)

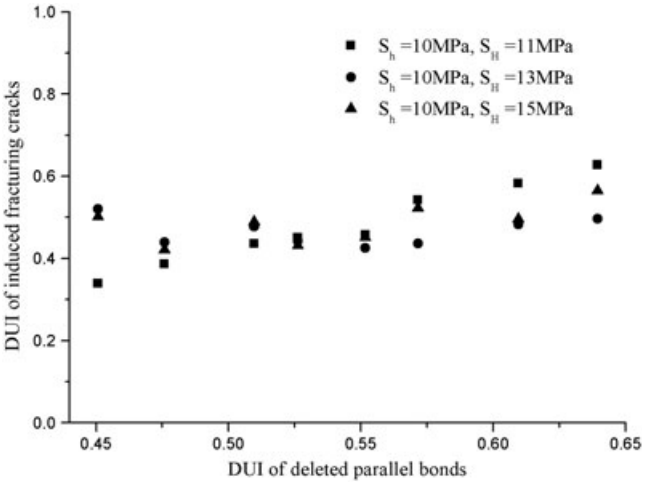

FIGURE 21 Distribution uniformity index (DUI) of induced fracturing cracks (horizontal stress ratio = 1.1, 1.3, and 1.5)

6 | CONCLUSIONS

The electron microscopic characteristics demonstrate that there are a large number of microcracks in shale. Because of the small size of the natural microcracks, they are generally treated as micropores in seepage calculation, which has only a slight direct effect on the seepage flow. However, these natural microcracks are widely distributed, which weakens the physical integrity of the rock and affects the macroscopic fracture propagation. Because the rock is modeled at the microscale in PFC3D, this characteristic of microcracks can be simulated precisely. Based on the shale mechanical parameters obtained from laboratory tests, we set up a numerical model in PFC3D. The influence of different crack distributions (the total number and DUI of microcracks) on the mechanical properties of shale was calculated. We mainly discussed the influence of different fracturing fluid viscosities (a viscosity of 0.02 m Pa s represents supercritical carbon dioxide, and a viscosity of 100 m Pa s represents the common hydraulic fracturing fluid) on the cumulative number and distribution uniformity of induced cracks, and we compared the relative relationship between the DUI of the initial microcracks and the DUI of the induced fractures. The results are summarized as follows:

1. The total number and DUI of microcracks have a significant influence on the mechanical properties of shale. The elastic modulus, UCS, and tensile strength decrease considerably with an increasing cumulative number of microcracks. The tensile strength increases with increases in the DUI when the total number of microcracks remains the same.
2. When the other conditions are the same, the DUI of the induced cracks of supercritical carbon dioxide fracturing is considerably larger than that of the common hydraulic fracturing and the increase trend is more notably with increases in the DUI of the initial microcracks. A larger DUI indicates that the distribution of cracks is more uniform and the induced cracks are more complex with multiple branches. This result demonstrates that the oil and gas recovery effect of supercritical carbon dioxide fracturing is better than that of hydraulic fracturing under certain conditions.
3. The effect of the initial DUI on the DUI of induced cracks is only obvious when the horizontal stress ratio is relatively small. With a higher horizontal stress ratio, the DUI of induced cracks is not sensitive to the initial microcracks' DUI; it does not increase and is always a single pattern. On the volume fracturing, both the horizontal stress ratio and uniform distribution of microcracks are important to form highly complex cracks.

The productivity of a shale reservoir after a fracturing stimulation is closely related to the distribution of the induced fracture network. The numerical model of supercritical CO_2 fracturing in this paper considered the effect of the special physical properties of the supercritical carbon dioxide (ie, ultra-low viscosity, high density, and other properties) on the distribution of the induced cracks. The seepage flow calculation of the model is simple, and the special percolation behavior of supercritical carbon dioxide is not considered. However, the model is of greater significance when introduced to obtain the rule of the induced cracks' distribution when the total number and distribution of microcracks are different for the sake of comparative studies. The simulation results show that the distribution uniformity of natural microcracks significantly affects the characterization of induced fractures. Additionally, the DUI does not impact the values of Young modulus and Poisson ratio. Therefore, in addition to the elastic modulus and Poisson ratio of rock, the DUI of natural microcracks should be taken into account in predicting the characteristics of supercritical CO_2 fracturing. It is necessary and significant to consider the influence of initial natural microcracks on the induced crack propagation and distribution.

However, simulation of fracturing with BPM method also has its shortcomings. To study the evolution of microcracks (microncracks and even nanocracks), the particle should be very small. Using a large-scale model will lead to a very large number of particles. Limited by the storage space and computing power of the computer, large-scale engineering problems cannot be simulated. The laboratory-scale model is affected by the boundary conditions, and some errors may occur compared with engineering practice. Although the continuum-type method has no model size problem, it is not very good at simulating microscopic mechanisms (such as the evolution of microcracks). The computational framework presented by Tjioe and Borja can accommodate the presence of pores in the solid and the stress concentrations that develop in the edges and corners of the pores and capture the microfracture processes.[41,42] Pore-scale modeling approaches are indeed very good methods that can address not only large-scale engineering but also micromechanisms. We will pay close attention to this method and combine discrete element method and pore-scale modeling approaches to establish the multiscale model of a fractured reservoir to study the fracturing problem for future study.

ACKNOWLEDGEMENTS

The authors gratefully acknowledge financial support from the National Natural Science Foundation of China (grants 51374213, 51674251, and 51608301), the National Natural Science Fund for Distinguished Young Scholars of China (grant 51125017), the Fund for Innovative Research and Development Group Program of Jiangsu Province (grant 2014-27), the

Priority Academic Program Development of Jiangsu Higher Education Institutions (grant PAPD 2014), the Foundation of Science Project of Beijing Municipal Education Commission (grant SQKM201610016015), and the China Postdoctoral Science Foundation (grant nos 2015M571030 and 2016M601170).

REFERENCES

1. Bennour Z, Ishida T, Nagaya Y, et al. Crack extension in hydraulic fracturing of shale cores using viscous oil, water, and liquid carbon dioxide. *Rock Mech Rock Eng*. 2015;48:1463-1473.
2. Zhang B, Li X, Zhang Z, Wu Y, Wu Y, Wang Y. Numerical investigation of influence of in-situ stress ratio, injection rate and fluid viscosity on hydraulic fracture propagation using a distinct element approach. *Energies*. 2016;9:1-19.
3. Ishida T, Aoyagi K, Niwa T, et al. Acoustic emission monitoring of hydraulic fracturing laboratory experiment with supercritical and liquid CO2. *Geophys Res Lett*. 2012;39:L16309.
4. Chen Y, Nagaya Y, Ishida T. Observations of fractures induced by hydraulic fracturing in anisotropic granite. *Rock Mech Rock Eng*. 2015;48:1455-1461.
5. Gan Q, Elsworth D, Alpern JS, Marone C, Connolly P. Breakdown pressures due to infiltration and exclusion in finite length boreholes. *J Petrol Sci Eng*. 2015;127:329-337.
6. He Z, Tian S, Li G, Wang H, Shen Z, Xu Z. The pressurization effect of jet fracturing using supercritical carbon dioxide. *J Nat Gas Sci Eng*. 2015;27:842-851.
7. Wang H, Li G, Tian S, Cheng Y, He Z, Yu S. Flow field simulation of supercritical carbon dioxide jet: comparison and sensitivity analysis. *J Hydrodyn Ser B*. 2015;27:210-215.
8. Jiang Y, Luo Y, Lu Y, Qin C, Liu H. Effects of supercritical CO_2 treatment time, pressure, and temperature on microstructure of shale. *Energy*. 2016;97:173-181.
9. Skurtveit E, Aker E, Soldal M, Angeli M, Wang Z. Experimental investigation of CO_2 breakthrough and flow mechanisms in shale. *Pet Geosci*. 2012;18:3-15.
10. Gale JFW, Reed RM, Holder J. Natural fractures in the Barnett Shale and their importance for hydraulic fracture treatments. *AAPG Bull*. 2007;91:603-622.
11. Ren L, Su Y, Zhan S, Hao Y, Meng F, Sheng G. Modeling and simulation of complex fracture network propagation with SRV fracturing in unconventional shale reservoirs. *J Nat Gas Sci Eng*. 2016;28:132-141.
12. Yushi Z, Shicheng Z, Tong Z, Xiang Z, Tiankui G. Experimental investigation into hydraulic fracture network propagation in gas shales using CT scanning technology. *Rock Mech Rock Eng*. 2015;49:33-45.
13. Zhao J, Li Y, Wang S, Jiang Y, Zhang L. Simulation of complex fracture networks influenced by natural fractures in shale gas reservoir. *Natural Gas Industry B*. 2014;1:89-95.
14. Zhang Q, Liu R, Pang Z, Lin W, Bai W, Wang H. Characterization of microscopic pore structures in lower Silurian black shale(S1l), southeastern Chongqing, China. *Mar Pet Geol*. 2016;71:250-259.
15. Liang L, Xiong J, Liu X. Mineralogical, microstructural and physiochemical characteristics of organic-rich shales in the Sichuan Basin, China. *J Nat Gas Sci Eng*. 2015;26:1200-1212.
16. Zeng W, Zhang J, Ding W, et al. Fracture development in Paleozoic shale of Chongqing area (South China). Part one: fracture characteristics and comparative analysis of main controlling factors. *J Asian Earth Sci*. 2013;75:251-266.
17. Nara Y, Meredith PG, Yoneda T, Kaneko K. Influence of macro-fractures and micro-fractures on permeability and elastic wave velocities in basalt at elevated pressure. *Tectonophysics*. 2011;503:52-59.
18. Hamidi F, Mortazavi A. A new three dimensional approach to numerically model hydraulic fracturing process. *J Petrol Sci Eng*. 2014;124:451-467.
19. Zou Y, Zhang S, Ma X, Zhou T, Zeng B. Numerical investigation of hydraulic fracture network propagation in naturally fractured shale formations. *J Struct Geol*. 2016;84:1-13.
20. Zhang Z, Li X, Yuan W, He J, Li G, Wu Y. Numerical analysis on the optimization of hydraulic fracture networks. *Energies*. 2015;8:12,061-12,079.
21. Nagel NB, Sanchez-Nagel MA, Zhang F, Garcia X, Lee B. Coupled numerical evaluations of the geomechanical interactions between a hydraulic fracture stimulation and a natural fracture system in shale formations. *Rock Mech Rock Eng*. 2013;46:581-609.
22. Ju Y, Liu P, Chen J, Yang Y, Ranjith PG. CDEM-based analysis of the 3D initiation and propagation of hydrofracturing cracks in heterogeneous glutenites. *J Nat Gas Sci Eng*. 2016;35:614-623.
23. Liu P, Ju Y, Ranjith PG, Zheng Z, Chen J. Experimental investigation of the effects of heterogeneity and geostress difference on the 3D growth and distribution of hydrofracturing cracks in unconventional reservoir rocks. *J Nat Gas Sci Eng*. 2016;35:541-554.

24. Duan K, Kwok CY, Pierce M. Discrete element method modeling of inherently anisotropic rocks under uniaxial compression loading. *Int J Numer Anal Methods Geomech*. 2016;40:1150-1183.

25. Samimi S, Pak A. A fully coupled element-free Galerkin model for hydro-mechanical analysis of advancement of fluid-driven fractures in porous media. *Int J Numer Anal Methods Geomech.* 2016;40:2178-2206.

26. Settgast RR, Fu P, Walsh SDC, White JA, Annavarapu C, Ryerson FJ. A fully coupled method for massively parallel simulation of hydraulically driven fractures in 3-dimensions. *Int J Numer Anal Methods Geomech.* 2017;41:627-653.

27. Itasca Consulting Group, Inc. PFC3D (particle flow code in 3 dimensions), Version 5.0; Itasca Consulting Group, Inc.: Minneapolis, MN, USA, 2014.

28. Yang J, Fu Y, Chen H, Zeng L, Li J. Rock mechanical characteristics of shale reservoirs. *Nat Gas Ind*. 2012;32: 12-14+100.

29. Cheung LYG, O'Sullivan C, Coop MR. Discrete element method simulations of analogue reservoir sandstones. *Int J Rock Mech Min Sci*. 2013;63:93-103.

30. Ghazvinian A, Sarfarazi V, Schubert W, Blumel M. A study of the failure mechanism of planar non-persistent open joints using PFC2D. *Rock Mech Rock Eng.* 2012;45:677-693.

31. Manouchehrian A, Sharifzadeh M, Marji MF, Gholamnejad J. A bonded particle model for analysis of the flaw orientation effect on crack propagation mechanism in brittle materials under compression. *Archives of Civil and Mechanical Engineering*. 2014;14:40-52.

32. Cho N, Martin CD, Sego DC. A clumped particle model for rock. *Int J Rock Mech Min Sci*. 2007;44:997-1010.

33. Asadi MS, Rasouli V, Barla G. A bonded particle model simulation of shear strength and asperity degradation for rough rock fractures. *Rock Mech Rock Eng.* 2012;45:649-675.

34. Yang S, Tian W, Huang Y, Ranjith PG, Ju Y. An experimental and numerical study on cracking behavior of brittle sandstone containing two non-coplanar fissures under uniaxial compression. *Rock Mech Rock Eng.* 2015;49:1497-1515.

35. Fjar E, Holt RM, Horsrud P, Raaen AM, Risnes R. *Petroleum Related Rock Mechanics*. 2nd ed. Amsterdam, The Netherlands: Elsevier Science; 2008.

36. Hazzard JF, Young RP, Oates SJ. Numerical modeling of seismicity induced by fluid injection in a fractured reservoir. In Proceedings of the 5th North American Rock Mechanics Symposium Mining and Tunnel Innovation and Opportunity, Toronto, ON, Canada, 7-10 July, 2002, 1023-1030.

37. Al-Busaidi A, Hazzard JF, Young RP. Distinct element modeling of hydraulically fractured Lac du Bonnet granite. *J Geophys Res Solid Earth*. 2005;110(B6):1-14.

38. Tomac I, Gutierrez M. Coupled hydro-thermo-mechanical modeling of hydraulic fracturing in quasi-brittle rocks using BPM-DEM. *J Rock Mech Geotech Eng*. 2017;9:92-104.

39. Damjanac B, Cundall P. Application of distinct element methods to simulation of hydraulic fracturing in naturally fractured reservoirs. *Comput Geotech*. 2016;71:283-294.

40. Liu X, Wang S, Wang S, Wang E. Fluid-driven fractures in granular materials. *Bull Eng Geol Environ*. 2015;74:621-636.

41. Tjioe M, Borja RI. On the pore-scale mechanisms leading to brittle and ductile deformation behavior of crystalline rocks. *Int J Numer Anal Methods Geomech.* 2015;39:1165-1187.

42. Tjioe M, Borja RI. Pore-scale modeling of deformation and shear band bifurcation in porous crystalline rocks. *Int J Numer Methods Eng*. 2016;108:183-212.

How to cite this article: Peng P, Ju Y, Wang Y, Wang S, Gao F. Numerical analysis of the effect of natural microcracks on the supercritical CO_2 fracturing crack network of shale rock based on bonded particle models. *Int J Numer Anal Methods Geomech*. 2017;1–23. https://doi.org/10.1002/nag.2712